


ORIGINAL RESEARCH

Automatic defect identification of PV panels with IR images through unmanned aircraft

Cheng Tang¹  | Hui Ren¹ | Jing Xia² | Fei Wang¹ | Jinling Lu¹

¹Department of Electrical Engineering, North China Electric Power University, Baoding, China

²State Grid Anqing Power Supply Company, Anqing, Anhui, China

Correspondence

Hui Ren, No.619 Yonghua North Street, Lianchi District, Baoding City, Hebei Province, China.
Email: hren@ncepu.edu.cn

Abstract

In order to improve the reliability and performance of photovoltaic systems, a fault diagnosis method for photovoltaic modules based on infrared images and improved MobileNet-V3 is proposed. Firstly, the defect images of open-source photovoltaic modules and their existing problems are analysed; based on the existing problems, image enhancement and data enhancement are performed on the infrared defect images of photovoltaic modules, so that the infrared images meet the requirements of image availability and sample quantity. Finally, the basic MobileNet-V3 network is improved to realize fault classification of photovoltaic modules. The experimental results show that, compared with the traditional CNN and the basic MobileNet V3, the proposed fault classification method not only has high accuracy and fast diagnosis speed, but also has a high recognition rate for various fault categories, which has good practicability and application value.

1 | INTRODUCTION

Deployment of solar photovoltaics (PV) has increased exponentially in the past years. Newly installed solar capacity is projected to reach 341 GW in 2023, reflecting a growth rate of 43 per cent compared to the 239 GW installed in 2022, according to a report from Solar Power Europe [1]. Defects of PV modules is inevitable since PV modules usually operate under harsh outdoor environmental conditions. Researchers have reported adverse effects of dust, dirt, pollution, bird droppings etc. on the PV module surface on the PV system output [2]. The appearance of defects in one cell has the potential to reduce the performance of the respective string, eventually, the performance and profitability of the PV system is affected [3, 4], even more serious safety hazards happen. Hence, it is imperative to detect and diagnosis the faulty photovoltaic modules timely for improving the operation and maintenance level of photovoltaic power plants, further tapping into their power generation capacity, and achieving sustainable development of green electricity [5].

Defects on PV modules cause temperature differences and based on this, different types of defects can be identified through the inspection of temperature distribution [6]. IR imaging provides a real-time two-dimensional image of PV module from which temperature distribution of the module surface can

be assessed [7]. With the development of drone applications, Remotely Piloted Aircraft (RPA) equipped with infrared camera equipment have become an effective mean of obtaining infrared images/videos of large-scale PV power plant photovoltaic modules due to their ability to control shooting angles and heights by planning flight routes. Moreover, RPA based IR imaging offers low inspection time, ease of access, high frequency of observations, and has the potential to reduce the operation and maintenance costs [8, 9].

Using RPA and IR for the inspection and fault diagnosis of PV modules follows several steps given by Figure 1 and depends on two main technologies: The first is collecting IR images through RPA, the second key technology include PV modules' anomaly detection and defect classification based on IR images.

For obtaining IR images through RPA, different environmental stress factors, such as weather, air turbulence and sunlight reflection, can influence the inspection and, consequently, the quality of the a 1RI images. Reference [9] provided a broad overview on the instrumentations, that is, RPA and thermal camera, that are required for the inspection of PV systems using RPA based IR imaging technology. Also, an extended review on RPA based IR imaging is presented by [11]. Multiple studies and practical practices have confirmed the feasibility of RPA-IR image-based identification and location of defective PV modules, especially the application in large scale PV stations [10].

This is an open access article under the terms of the [Creative Commons Attribution](https://creativecommons.org/licenses/by/4.0/) License, which permits use, distribution and reproduction in any medium, provided the original work is properly cited.

© 2023 The Authors. *IET Renewable Power Generation* published by John Wiley & Sons Ltd on behalf of The Institution of Engineering and Technology.

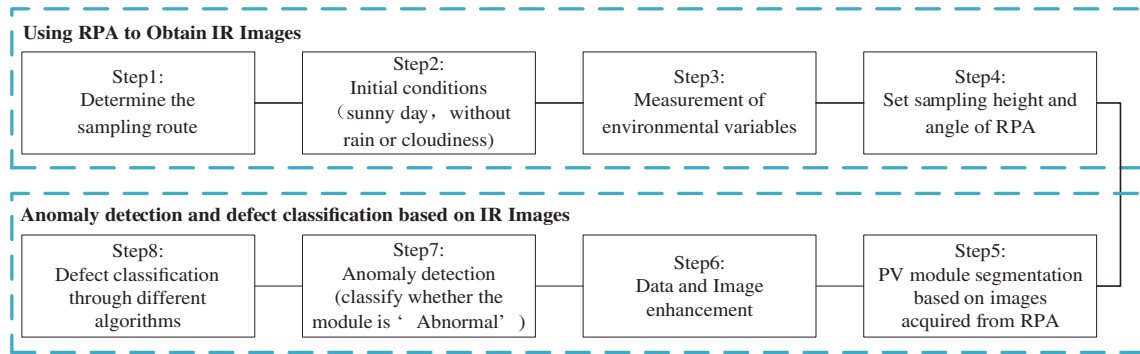


FIGURE 1 Steps of using RPA and IR for PV module fault diagnosis.

Practical considerations, such as flight height [8, 12], horizontal distance [13], angle [12, 13] of observation, camera resolution [23], sampling time [31] and environment requirements [8], which influence the inspection and consequently the quality of the IR images have been addressed by multiple researches [12, 33, 34].

For anomaly detection and defect classification, with the development of machine learning algorithms [28], ResNet [10, 19], R-CNN [14], BP [15], VGG-16 [16], CNN [18] have been widely used in fault diagnosis and defects classification of photovoltaic modules based on infrared images. With the emergence of new machine learning networks, improvements are made in regard to classification accuracy and lightweight. Special issues that cannot be avoided when filming, such as the reflection of sun spots and flare, can also be removed with the aid of computer algorithms and the identification of light perception [21, 22].

Machine learning based defects classification depends on the dataset. Due to the fact that defects are relatively rare compared to normal modules, the number of images of faulty PV components is limited and unbalanced. Scale invariant feature transform [16], generative adversarial nets [17], vertical and horizontal flipping method [18] are used to expand the dataset, enabling diagnostic models to be fully trained. Although these data enhancement methods can solve the problem of unbalanced datasets, these methods rely heavily on the original data set and have poor performance face up to adversarial examples, the generated images may be over-fitting also.

To improve fault recognition based on IR images, future breakthroughs can be summarized as follows:

- IContinuously improve the database of abnormal modules;
- IIExplore more effective (higher accuracy, more lightweight) multi-classification algorithm.

Based on the understanding of previous research, the contribution of this study is given below:

1. According to the characteristics of low contrast and unbalanced number of images in the dataset, the histogram equalization and Mixup method are used to enhance the quality of infrared images of PV modules, thereby improving

the accuracy of PV module fault diagnosis based on infrared images and deep learning methods.

2. The lightweight network MobileNet-V3 is improved according to the characteristics and requirements of the application, which can reduce the model parameters, computational cost and improve the diagnostic speed under the premise of ensuring the accuracy of the model.

2 | DATA SET FOR DEFECT CLASSIFICATION













The proposed research is based on the dataset published by Raptor Maps, a company that develops lifecycle management software for PV plants [30]. Its development team collects infrared images of actual PV modules in operation, diagnoses them and labels them to support its lifecycle management software for photovoltaic plants. Each image in the dataset is taken by a drone system equipped with a medium-wave or long-wave infrared camera (3–13.5 μm). The dataset includes 10,000 labelled thermal images of modules of 11 different faults and 10,000 thermal images of normal modules. It is so far the best dataset for studying the fault identification method of photovoltaic modules based on deep learning.

By analysing the dataset, we found that there are still two major problems with the dataset.

2.1 | Greyscale image with low contrast

Table 1 gives the information of the original defect/normal IR images of PV modules given in reference [30]. The intensity range of the grayscale IR images is limited, showing a very low contrast effect. We use grey entropy to quantify the amount of information contained in the image, and the calculation result shows a lack of detail and clarity of features. Since the IR image is obtained by ‘measuring’ the amount of heat radiated outward from the object. One of the defects that cannot be avoided in infrared images is the defective sample and interfering information contained in the RGB or thermal image hinder the model from learning proper saliency features [19].

TABLE 1 Open-source photovoltaic module defect images and explanation of the defect classes.

| Defects classes | Image | Volume | Intensity | Grey entropy | Explanation |
|-----------------|-------------------------------------------------------------------------------------|------------|---------------|--------------|-----------------------------------------------------------------------------------------------------------------------------------------------------------------------------------------------------------------------------|
| Off-line module |  | 828 | 25.35–171.65 | 6.36 | Photovoltaic module is disconnected. |
| Diode |  | 1499 | 125.65–243.35 | 5.97 | Bypass diodes perform the function of providing a bypass path for the current flow. |
| Diode multi |  | 175 | 71.05–197.95 | 5.50 | Multiple bypass diode damage. |
| Cell |  | 1877 | 83.15–255 | 6.68 | Single cell with difference in temperature in a rectangular format. |
| Cell multi |  | 1288 | 80.80–253 | 6.23 | Multiple cells with difference in temperature in a rectangular format. |
| Hot spot |  | 251 | 144.75–240.25 | 6.23 | Snail trails and discoloration. |
| Hot spot multi |  | 247 | 83.15–252.85 | 6.68 | Multiple snail trails and discoloration. |
| Crack |  | 941 | 97.30–253 | 6.68 | Appearing in the system as micro cracks or broken cells. |
| Soiling |  | 205 | 108.45–252.56 | 5.74 | Soiling refers to power loss resulting from snow, dirt, dust and other particles that cover the surface of the PV module [20]. |
| Vegetation |  | 1739 | 11.79–253 | 5.59 | Plants cover the surface of photovoltaic modules. |
| Shadowing |  | 1056 | 142.0–230.0 | 5.82 | The shaded modules receive lesser irradiation than the unshaded modules of the PV array [24]. In a shading condition, the maximum power of a PV module can drop significantly reducing the energy yield of the system [25]. |
| No anomaly |  | 10,000 | 113.35–193.66 | 5.25 | Images without fault. |

The grey entropy is calculated by (1)

$$H = - \sum_{i=0}^{n-1} p_i \log p_i \quad (1)$$

where p_i is the probability of grey level i of the image. When the image grey level values are uniformly distributed between 0 and 255, the corresponding entropy is the maximum, and the image has the highest contrast, showing the most obvious detail information and the best overall image quality.

2.2 | Imbalance of dataset with different fault categories

Among the 11 types of fault samples, the number of different fault categories varies greatly, with some fault categories having only 175 images while some fault categories having as many as 1877. The imbalance will lead to large differences in performance among various classes.

2.3 | Infrared image enhancement based on histogram equalization

Contrast is defined as the difference in intensity between two objects in an image. If the contrast is too low, it is impossible to distinguish between two objects not to mention more types of objects, which means they will be seen as a single object.

Grayscale differences among images are generally quantified by Grayscale Entropy. The higher the grey-scale entropy, the higher the image contrast. From Equation (1), it can be seen that increasing the range of grey scale distribution can increase the grey scale entropy and achieve the effect of enhancing the image contrast.

Histogram equalization is a widely used contrast-enhancement technique in image processing because of its high efficiency and simplicity. It is one of the sophisticated methods for modifying the dynamic range and contrast of an image by altering that image such that its intensity histogram has the desired shape.

Using the histogram equalization method [29], the original image with a non-uniform distribution of the grey range is mapped with a cumulative distribution function of the probability of each grey level to obtain an image with a uniform grey distribution.

Let f be a given IR image represented as an m by n matrix of integer pixel intensities ranging from 0 to $L-1$. L is the number of possible intensity values. Let p denote the normalized histogram of f with a bin for each possible intensity. So

$$P_n = \frac{\text{number of pixels with intensity } n}{\text{total number of pixels}} \quad n = 0, 1, \dots, L-1 \quad (2)$$

The pixel intensity is transformed to s_k by the following function:

$$S_k = \text{floor}[(L-1) \sum_{n=0}^k P_n] \quad (3)$$












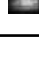
After image enhancement of histogram equalization, the range of the original greyscale image increases, maximizing the grayscale entropy of the IR image and increasing the image's contrast. The concrete enhancement effect is given in Table 2.

2.4 | Data enhancement based on Mixup

In the data set, defects of diode multi, hot spot, hot spot multi, and soiling all have sample images less than 500, and comparing with the normal samples, which reaches 10,000, the unbalance among different sets cannot be ignored (see the third column of Table 1).

The solution to the imbalance in such datasets is generally to increase the number of samples in small categories by means of data enhancement. Data augmentation methods can be classified as both same-class augmentation (geometric transformation of images) and mixed-class augmentation (generative adversarial networks, Mixup, Cut mix etc.). Although the same class data enhancement method can solve the problem of

TABLE 2 Data set image enhancement effects.

| Defects classes | Image enhanced | Intensity | Grey entropy |
|-----------------|---------------------------------------------------------------------------------------|-----------|--------------|
| Off-line module |  | 0–255 | 7.78 |
| Diode |  | 0–255 | 7.81 |
| Diode multi |  | 0–255 | 7.75 |
| Cell |  | 0–255 | 7.80 |
| Cell multi |  | 0–255 | 7.78 |
| Hot spot |  | 0–255 | 7.80 |
| Hot spot multi |  | 0–255 | 7.81 |
| Crack |  | 0–255 | 7.81 |
| Soiling |  | 0–255 | 7.77 |
| Vegetation |  | 0–255 | 7.73 |
| Shadowing |  | 0–255 | 7.82 |
| No anomaly |  | 0–255 | 7.72 |

unbalanced datasets, it relies heavily on the original dataset. In contrast, Mixup [35], a mixed-class data augmentation method based on the neighbourhood risk principle, fuses images through simple linear interpolation to construct virtual samples, which can improve the model's ability to adapt to non-trained samples, enhance the linear representation between samples, improve the model's uncertainty estimation ability, and enable the neural network's generalisation ability to be improved. Compared with large deep neural network methods such as generative adversarial networks, it can avoid the disadvantages of huge memory loss and less desirable sensitivity to samples (see Table 3).

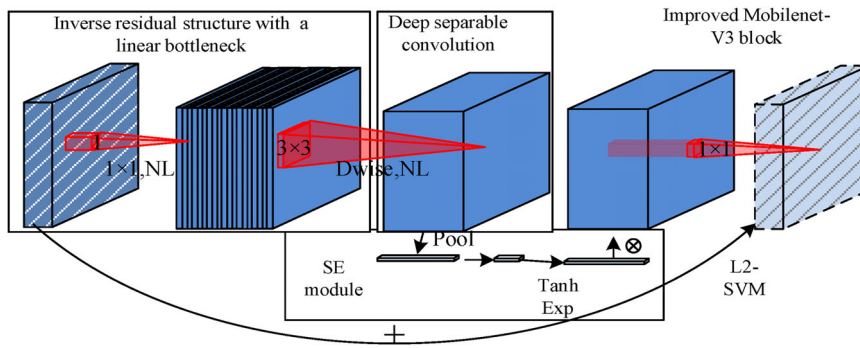
3 | DIAGNOSE MODELS AND EVALUATION INDICATORS

3.1 | Introduction to MobileNet-V3

Choosing the MobieNetV3 as the basis of the image recognition model can invoke deep separable convolution and 1×1 lifting dimensional layers. It also offers high accuracy with a low

TABLE 3 Infrared patterns expended by different data augmentation methods.

| Class | Original image and image after geometric transformation | Expand data set through simple geometric transformation | Original image and Mixup expanded image | Expand the dataset through Mixup |
|--------------------|---------------------------------------------------------|--------------------------------------------------------------------------------------------------------------------------------------------------------------------------------------------------------------------|-----------------------------------------|--------------------------------------------------------------------------------------------------------------------------------------------------------------------------------|
| Diode /Diode Multi | | When the image of the bypass diode fault is symmetrical, the expansion may be repeated with the original image through simple geometric transformation, and the task of expanding the data set cannot be realized. | | Mixup fuses images through linear interpolation, which can fully avoid image repetition. |
| Cell/Cell Multi | | For the hot spot fault, the data enhanced by simple geometric transformation may not conform to the original sample distribution or be independent of the original sample. | | Mixup supplements the image by interpolation, which is closely related to the original image distribution and more consistent with the original characteristics of the sample. |
| Soiling | | After simple geometric transformation, the spots in the image only change the position, but the size does not change, which may not be a good expansion of the data set. | | Mixup can generate various speckles of different sizes through interpolation, making the dataset richer. |

**FIGURE 2** Improved bneck structure.

number of parameters and operations and can be easily deployed in environments with insufficient hardware [26, 36]. At the same time, the attention mechanism is introduced to obtain a high degree of adaptability to the output weights of different layers, which improves the accuracy of the model to a certain extent. Reference [32] provides a specific explanation of the structure of MobileNet-V3.

The core of MobileNet-V3 is the bneck structure, as shown in Figure 2. The core components include a deep separable convolution, an inverse residual structure with a linear bottleneck and an attention mechanism (SE) module. With the support of the above structure, the speed of fault diagnosis is greatly improved, and the model can learn more detailed picture features to improve the accuracy of classification.

3.1.1 | Deeply separable convolution

The core idea of the MobileNet series is to replace the standard convolution with a deeply separable convolution. The depth separable convolution is calculated in two stages: in the first

stage, a convolution filter is applied to each input channel. In the second stage, a point-by-point convolution (1 convolution) is applied to all output channels of deep convolution [36]. The above method can reduce the amount of calculation and parameters, shorten the training time, and significantly improve the speed of fault diagnosis, but the diagnostic accuracy is slightly reduced.

Assuming that the input feature map dimension is (D_F, D_F, M) , the convolution kernel is (N, D_K, D_K, M) , and the output feature dimension is (D_G, D_G, N) .

The computational and parametric quantities of the standard convolution are

$$P_1 = D_G \cdot D_G \cdot D_K \cdot D_K \cdot N \cdot M \quad (4)$$

$$C_1 = (D_K \cdot D_K \cdot M) \cdot N \quad (5)$$

The depth-separable convolutional computation and the number of parameters are

$$P_2 = D_G^2 \cdot D_K \cdot M + D_G^2 \cdot M \cdot N \quad (6)$$

$$C_2 = D_K^2 + M \cdot N \quad (7)$$

The ratio of the two calculated, parametric quantities is

$$\frac{P_2}{P_1} = \frac{C_2}{C_1} = \frac{1}{N} + \frac{1}{D_K^2} \quad (8)$$

In real networks, N is taken to be much larger than D_K^2 and it can be seen from Equation (8) that the depth-separable convolution method can reduce the computation and number of parameters by a factor of D_K^2 compared to the standard convolution method, thus greatly reducing the training time.

3.1.2 | Inverse residual structure with linear bottleneck

Photovoltaic module defect infrared image contrast is low, need to be able to learn more details of the photovoltaic module defect structure, so as to improve the defect classification accuracy. The 'linear bottleneck' of MobileNet-V3 is a convolutional layer with filters that combines linear functions. This structure has three main advantages: (a) it increases the dimensionality of the input feature map, allowing the model to learn more features, thus improving the performance of the model. (b) It overcomes the problem of gradient disappearance at deeper layers of the network by using skip connection technology, thereby accelerating the training speed. (c) Mapping the feature maps from the convolutional layer to the deconvolutional layer allows for more detailed image detail information.

3.1.3 | SE modules

The SE module makes the model focus on more useful features by assigning different weights to each feature map.

3.2 | Introduction to improved MobileNet-V3

In order to further improve the accuracy and computational speed of fault classification, this paper improves the network by optimising the activation function and classifier on the basis of MobileNet-V3 Large.

3.2.1 | Activation function optimisation

The activation function is an important aspect of a neural network, which determines the learning ability of the network. In the basic MobileNetV3 model, H-Swish [37] is used as the activation function. Given the large amount of data and the variety of classifications of PV module defect images, an activation function with higher efficiency, stronger robustness and as simple as possible than H-Swish is needed. Based on this,

the TanhExp [38] activation function is chosen instead of the H-Swish activation function in this paper.

Definition of TanhExp.

$$F(x) = x \text{Tanh}(\text{Exp}(x)) \quad (9)$$

Of which, $\tanh(x) = \frac{e^x - e^{-x}}{e^x + e^{-x}}$.

TanhExp has the following features: firstly, TanhExp is a continuous function with negative values and an approximately linear positive part, which solves the problem of vanishing gradients and increases the speed of convergence; secondly, TanhExp shows a steeper gradient close to zero, which can accelerate the updating of parameters in the network, further speeding up the learning process; finally, TanhExp shows a particularly continuous and smooth transition shape. This property ensures that TanhExp can combine the advantages of both segmented and non-segmented activation functions and perform even better.

The above features allow the use of TanhExp as the activation function to improve the overall recognition rate of the model and to improve the diagnosis speed and classification accuracy of multiple classification.

3.2.2 | Classifier optimization

In the MobileNet-V3 model, SoftMax is used to complete the multi-classification process. Due to the low degree of differentiation between PV defect images and there up to 12 categories to be classified, SoftMax is prone to misjudgement. The L2-SVM algorithm [38] has better differentiability and strong generalisation performance in large data, multi-classification problems, which can greatly improve the recognition efficiency of the model and increase the classification accuracy. Therefore, in this paper, L2-SVM is used as a classifier to improve MobileNet-V3.

L2-SVM is an improved algorithm based on the SVM model. Given the training data $(x_n, y_n), n = 1, 2, \dots, N, x_n \in R^D, t_n \in \{-1, 1\}$, the constrained support vector machine SVM model is

$$\min_{\omega, \xi_n} \frac{1}{2} \omega^T \omega + C \sum_{i=1}^N \xi_n \quad (10)$$

$$s.t. \omega^T x_n t_n \geq 1 - \xi_n \forall n \quad (11)$$

$$\xi_n \geq 0 \forall n \quad (12)$$

where ξ_n is the slack variable, ω denotes the optimal hyperplane normal vector, and C represents the error weight used to adjust for misclassified samples.

The L2-SVM objective function is

$$\min_{\omega, \xi_n} \frac{1}{2} \omega^T \omega + C \sum_{i=1}^N \max(1 - \omega^T x_n t_n, 0) \quad (13)$$

For the test data, the predicted categories are

$$\arg \max_i (\omega^T x) f \quad (14)$$

3.3 | Evaluation indicators

In two-class classification, P is a positive sample, N is a negative sample, TP indicates a correct prediction of a positive sample, TN indicates a correct prediction of a negative sample, FP indicates an incorrect prediction of a negative sample as a positive sample, and FN indicates an incorrect prediction of a positive sample as a negative sample, the evaluation indicator formula is as follows.

$$\text{accuracy} = \frac{TP + TN}{P + N} \quad (15)$$

$$\text{precision ratio} = \frac{TP}{TP + FP} \quad (16)$$

$$\text{recall ratio} = \frac{TP}{TP + FN} \quad (17)$$

$$F_1 = \frac{2 \times \text{precision ratio} \times \text{recall ratio}}{\text{precision ratio} + \text{recall ratio}} \quad (18)$$

4 | SIMULATIONS

Using the data set provided by Raptor Maps [30], we first confirm the relevant indicators of Mixup data expansion, and then verify the diagnostic effect of Image enhancement. After that, we conducted three related diagnostic experiments, including the comparison of CNN [27], MobileNet-V3 and proposed Improved MobileNet-V3 on 2-class classification, performance analysis of the Improved MobileNet-V3 model on 11-class classification of PV modules and the influence of number of defects on the diagnosis effect.

4.1 | Parameter selection for image enhancement

The formula of Mixup is

$$\tilde{x}(a, b) = \lambda x_i(a, b) + (1 - \lambda) x_j(a, b) \quad (19)$$

where $x_i(a, b)$ and $x_j(a, b)$ are intensity of pixels from images randomly drawn from the same sample set, and $\lambda \in [0, 1]$ is the mixup strength. $\tilde{x}(a, b)$ is the intensity of pixel of new image created by mixup technique.

Using the hot spot fault as an example, Figure 3 shows the data enhancement effect of the Mixup algorithm for the original image and different mixing coefficients λ .

Figure 4 and Table 4 show the results of expanding four types of images with less than 500 images by using different λ values. By comparing the diagnostic accuracy with the confusion matrix, it is found that when $\lambda = 0.5$, the diagnostic error is

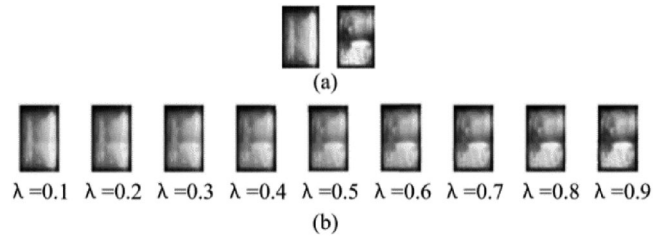


FIGURE 3 (a) Original image (b) Mixup algorithm data enhancement effect with different mixing coefficients λ .

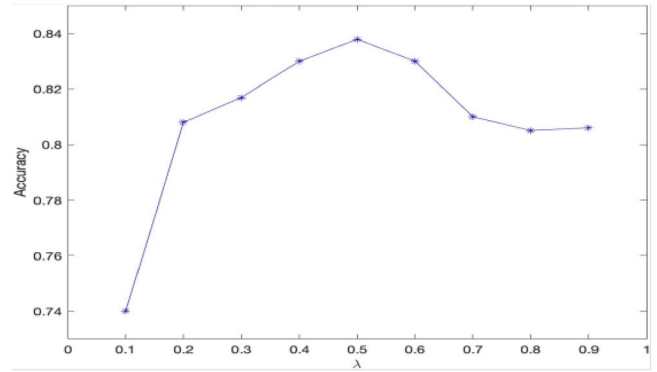


FIGURE 4 Diagnostic accuracy of different λ values.

the smallest (see Figure 4). Therefore, this paper applies Mixup to the aforementioned four categories of less than 500 samples, using $\lambda = 0.5$ for data augmentation until the dataset is expanded to 500 samples.

4.2 | The effect of image enhancement on the 6-classification performance of proposed model

The effect of image enhancement on the classification of 6 defects of PV modules is tested. Figures 5 and 6 show the confusion matrix with and without image enhancement. With image enhancement, an average accuracy of 85.17% is achieved, which is 12.34% higher than without image enhancement.

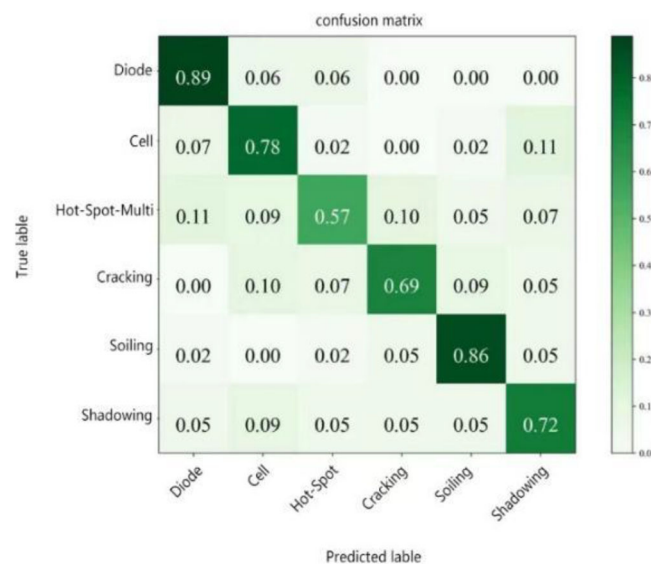
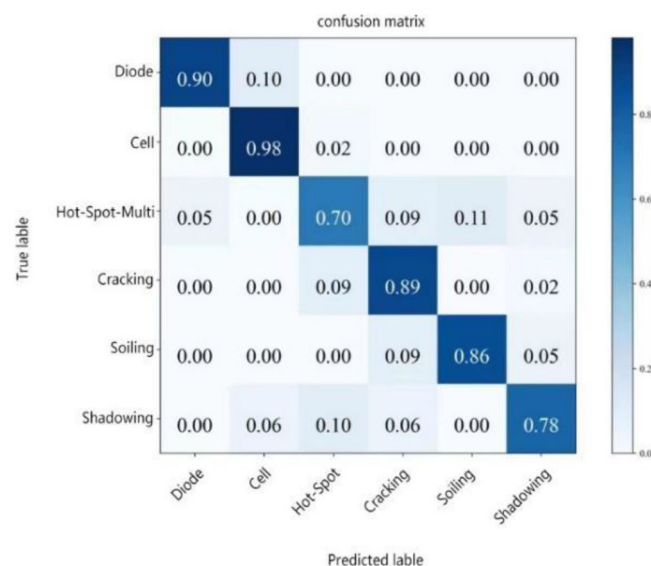
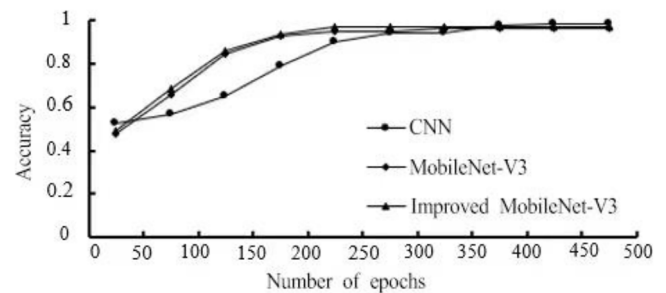
4.3 | Case 1: The comparison of CNN, MobileNet-V3 and proposed improved MobileNet-Vs

We compare the performance of CNN, MobileNet-V3 and the proposed improved MobileNet-V3 model for the detection of defects in PV modules.

The PV modules is classified as 'Normal' or 'Abnormal' by the proposed model in the paper. After image and data enhancement, dataset with failure images fewer than 500 are augmented to 500 images. From each dataset, 200 images are randomly selected, and a dataset with a total of 2200 abnormal thermal images is formed; while another 2200 images from the normal dataset are chosen to form the 'normal' dataset. 85% of them

TABLE 4 Mixup algorithm data enhancement effect with different mixing coefficients λ .

| λ | Diode multi | Hot spot | Diode | Hot spot multi | Shadowing | Soiling | Accuracy |
|-----------|-------------|----------|-------|----------------|-----------|---------|----------|
| 0.1 | 0.79 | 0.91 | 0.55 | 0.56 | 0.83 | 0.8 | 0.74 |
| 0.2 | 0.86 | 0.92 | 0.67 | 0.73 | 0.84 | 0.83 | 0.808 |
| 0.3 | 0.86 | 0.96 | 0.67 | 0.71 | 0.83 | 0.87 | 0.817 |
| 0.4 | 0.88 | 0.95 | 0.69 | 0.77 | 0.86 | 0.83 | 0.83 |
| 0.5 | 0.84 | 0.96 | 0.69 | 0.81 | 0.86 | 0.87 | 0.838 |
| 0.6 | 0.84 | 0.95 | 0.63 | 0.87 | 0.84 | 0.85 | 0.83 |
| 0.7 | 0.86 | 0.92 | 0.68 | 0.76 | 0.79 | 0.85 | 0.81 |
| 0.8 | 0.84 | 0.96 | 0.59 | 0.76 | 0.83 | 0.85 | 0.805 |
| 0.9 | 0.82 | 0.99 | 0.61 | 0.73 | 0.84 | 0.85 | 0.806 |

**FIGURE 5** The common fault classification result of the image without enhancement.**FIGURE 6** The common fault classification result after the image is enhanced.**FIGURE 7** Comparison of the accuracy along number of epochs among three models.**TABLE 5** Comparison of the training accuracy, training time and computational cost of different models for 2-class classification problem.

| | CNN [14] | MobileNet-V3 | Improved MobileNet-V3 |
|-------------------|-------------|--------------|-----------------------|
| Accuracy | 98.5% | 96.6% | 97.8% |
| Training time (h) | 5 | 3.8 | 3.5 |
| Parameters | 138,357,544 | 5,483,032 | 3,504,872 |
| FLOPs | 18.14G | 286.98 M | 403.37 M |
| MAdds | 36.22G | 565.78 M | 791.11 M |

are used for training, while the rest are used for testing. Three different deep learning models, that is, CNN [14], MobileNet-V3 [26], and the proposed improved MobileNet-V3, are trained 500 times and compared with regard to their detection accuracy and training speed.

We test the training speed and accuracy of CNN, MobileNet-V3 and proposed improved MobileNet-V3.

Figure 7 shows the accuracy of CNN converges after 400 training sessions, while those of MobileNet-V3 and improved MobileNet-V3 converge steadily after 250 trainings, which means the improved MobileNet-V3 model can reduced the training time by 30% compared to CNN model. The accuracy of the CNN model often fluctuated in the late training period, while the improved MobileNet-V3 model had almost no fluctuation. Table 5 gives a comparison of the classification

TABLE 6 Improved MobileNet-V3 detection results.

| | Precision | Recall | F1-score | No. of samples |
|--------------------|-----------|--------|----------|----------------|
| Model with anomaly | 96% | 94.12% | 95.05% | 2200 |
| No anomaly | 94% | 95.92% | 94.95% | 2200 |

accuracy, training time and computational cost of three different models, the indicators that measure the computational costs of deep learning algorithms include Parameters, FLOPs and MAdds [39]. We use torchstat in PyCharm to perform network parameter calculation. The comparison shows that with the improved MobileNet-V3 model, the accuracy of the classification was improved by 1.2% and the training speed was improved by 7% on top of the MobileNet-V3 model. The Improved MobileNet-V3 has significant advantages over CNN model and slightly better than MobilNet-V3 with regard to training speed and accuracy.

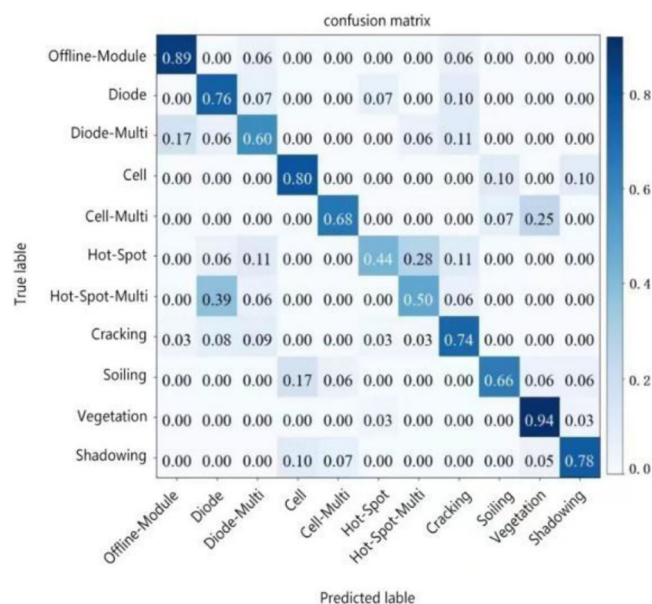
As can be seen in Table 6, the proposed model diagnosis has a 95% probability of correctly predicting whether a fault has occurred on the abnormality detection problem. The F1 values provide a comprehensive evaluation of the model's accuracy and recall ratio, reflecting the classifier performance. When classifying the test dataset, the model scores close to 95% on both the normal/abnormal categories of F1, indicating that the method has good classification performance.

4.4 | Case 2: performance analysis of the improved MobileNet-V3 model on classification of defects in PV modules

We test the performance of the proposed improved MobileNet-V3 model for the classification of 11 defects. The classification of 11 different categories of PV modules is performed. After image enhancement and data enhancement, 500 images from each of the 11 fault categories were randomly selected to create a balanced dataset with a total of 5500 IR images. 85% of them are used for training, while the rest are used for testing. The improved MobileNet-V3 network proposed in this paper was used to train 1000 times.

As can be seen in Table 7, the average accuracy of the model proposed in this paper is 70.82% for the 11-classification, while in reference [18], an average accuracy of 63.54% is achieved for the same problem by using of CNN method and MobileNet-V3, which is 7.28% lower than the proposed method.

Figure 8 gives the confusion matrix of the trained model in the test set of 11-classification. As seen in Figure 8, The accuracy of the proposed model can correctly classify some types of faults is about 80%, but there is still moderate confusion between some faults, such as hot spots and multiple hot spots, multi-hot spots and diode-multi, shadowing and multi-cell. Compared with reference [18], although our proposed

**FIGURE 8** 11-class confusion matrix under the improved MobileNet-V3 model.

method still has confusion between some categories, there are fewer categories with confusion.

Reasons for the confusion could be that: (a) the similar images of some fault categories vary greatly, which makes it difficult to train a model with high generalisation capability; (b) the poor differentiation of images between different fault categories, for example, cracking, soiling, vegetation and shadowing have a high within- and between-class variation that make it difficult to correctly classify a fault under an unbalanced dataset with a small number of cases for some classes [18], which is difficult to rely on infrared images alone to subdivision, requiring a combination of other methods, such as visible images etc. (c) Too many classification categories and a large amount of data may cause over-fitting of the model and affect the generalization ability. As can be seen in Table 8, when the number of classification categories is reduced and only the 6 common types of faults are classified, the accuracy rate is significantly improved.

4.5 | Case 3: Classification of defects in PV modules with reducing number of possible classes

The last proposed case evaluates the effect of some classes, with possibly high variation within and between classes, in the performance of the model.

Classes such as cracking, soiling, and vegetation that have a high variation of IR image patterns within their classes and between classes are eliminated to evaluate the effect of these classes on the classification performance of our proposed model. After eliminating the six mentioned classes. Six common types of faults, diode and diode multi, cell and cell multi, multiple hot spots, cracks, soiling, shadows, are selected to

TABLE 7 Improved MobileNet-V3 fault classification results for the 11-class classification.

| | Evaluating indicator | Off-line-module | Diode | Diode-multi | Cell | Cell-multi | Hot-spot | Hot-spot-multi | Cracking | Soiling | Vegetation | Shadowing |
|-------------------------|----------------------|-----------------|-------|-------------|-------|------------|----------|----------------|----------|---------|------------|-----------|
| 11-class classification | Precision% | 89.00 | 76.00 | 60.00 | 80.00 | 68.00 | 44.00 | 50.00 | 74.00 | 66.00 | 94.00 | 78.00 |
| | Recall% | 81.65 | 56.30 | 64.52 | 74.77 | 83.95 | 77.19 | 57.47 | 62.70 | 79.50 | 72.30 | 80.40 |
| | F1-score% | 85.17 | 64.68 | 62.18 | 77.30 | 75.14 | 56.05 | 53.47 | 67.89 | 67.89 | 81.73 | 78.19 |
| | Accuracy% | 70.82 | | | | | | | | | | |

TABLE 8 Improved MobileNet-V3 fault classification results for the 6-class classification.

| | Evaluating indicator | Diode | Cell | Hot-spot-multi | Cracking | Soiling | Shadowing |
|------------------------|----------------------|-------|-------|----------------|----------|---------|-----------|
| 6-class classification | Precision% | 90.00 | 98.00 | 70.00 | 89.00 | 86.00 | 78.00 |
| | Recall% | 94.74 | 85.97 | 76.92 | 78.76 | 88.67 | 86.67 |
| | F1-score% | 92.31 | 91.59 | 73.29 | 83.57 | 87.31 | 82.11 |
| | Accuracy% | 85.17 | | | | | |

form a sub dataset. Two datasets were constructed by original IR images with data enhancement only and with both data enhancement and image enhancement, respectively. Either dataset has 3000 IR images with random selected 500 images from each of the 6 fault categories. The dataset is divided to the training set and testing set according to a ratio of 85:15. The proposed improved MobileNet-V3 model is trained 1000 times.

The average classification accuracy of the six common fault categories is 85.17% (Figure 6), and the average accuracy of the six classifications was 14.27% higher than that of the 12 classifications. As can be seen from the cumulative F1 scores of the improved MobileNet-V3 algorithm's classification results for each fault category in Tables 7 and 8, the F1 scores were lower in the 11 fault categories, while in the common six fault categories, in the bypass diode damage, and battery temperature difference are above 90%, while F1 scores for multiple hot spots, cracks, fouling, plant cover, and shadows are relatively low, but also generally above 80%. It can be seen that the number of classification categories affects algorithm performance.

5 | CONCLUSION

Here, a fault diagnosis method for PV modules based on infrared images and improved MobileNet-V3 is proposed. Firstly, histogram equalization is used to enhance the infrared images of PV modules to improve the quality of infrared images; then, Mixup data enhancement is used to solve the problem of imbalanced datasets; finally, the advantages of fast fault diagnosis and high classification accuracy of improved MobileNet-V3 are used to diagnose PV module defects. By applying the methods in this paper to the infrared images of PV modules in actual operation provided by open-source dataset for simula-

tion experimental validation, the following conclusions can be drawn.

1. The histogram equalization method can be used to enhance the quality of infrared images of PV modules, thereby improving the accuracy of PV module fault diagnosis based on infrared images and deep learning methods.
2. The improved MobileNet-V3 model is slightly less accurate than the traditional CNN in diagnosing PV module anomalies, with a 97.8% probability of correctly identifying whether a module has failed, only 0.7% lower than the CNN model, but with a 30% reduction in training time compared to the CNN.
3. The improved MobileNet-V3 PV module fault diagnosis model was used to significantly improve the diagnostic accuracy of multiple anomalies in PV modules. In the diagnosis of 11 categories of anomalies, the accuracy reached 70.82%, which is 13.7% higher than the diagnostic accuracy of the CNN-based model. In the diagnosis of 6 categories of common abnormal components, the accuracy was 85.17%.

In conclusion, the training and test data used in this research are all infrared images of PV modules in actual operation. The analysis results show that the method in this paper outperforms similar published methods in terms of training speed and diagnostic accuracy, and has good application value.

AUTHOR CONTRIBUTIONS

Cheng Tang: Software, Validation, Visualization, Writing—original draft, Writing—review and editing; Hui Ren: Funding acquisition, Investigation, Methodology, Project administration; Jing Xia: Methodology, Resources, Writing—review and editing;

Fei Wang: Conceptualization, Project administration; Jinling Lu: Methodology, Project administration.

CONFLICT OF INTEREST STATEMENT

The authors declare no conflicts of interest.

FUNDING INFORMATION

This research did not receive any specific grant from funding agencies in the public, commercial, or not-for-profit sectors.

DATA AVAILABILITY STATEMENT

The data that support the findings of this study are available from the corresponding author upon reasonable request.

ORCID

Cheng Tang  <https://orcid.org/0000-0003-2932-8520>

REFERENCES

- IEA. Global market outlook for solar power 2023–2027. (2023). <https://www.solarpowerEurope.org/press-releases/46-gw-of-new-solar-power-in-2022-the-continent-celebrates-the-first-european-solar-day>
- Vinit, Y., Prajval, S., Indrajit, M., et al.: Cutting edge cleaning solution for PV modules. *Mater. Today: Proceedings* 39, 2005–2008 (2021)
- Dalsass, M., Scheuerpflug, H., Maier, M., Brabec, C.J., et al.: Correlation between the monitoring data of a photovoltaic power plant and module defects detected by dronemounted thermography. In: 31st European Photovoltaic Solar Energy Conference and Exhibition. pp. 1793–1798 (2015)
- Waqar Akram, M., Li, G., Jin, Y., et al.: Failures of photovoltaic modules and their detection: A review. *Appl. Energy* 313, 118822 (2022)
- Mavian, X., Grace, K., Lau Siu-Kit, T., et al.: Motivations and deterrents of Asian small and medium-sized enterprises' willingness to adopt green electricity. *J. Cleaner Prod.* 370, 133233 (2022)
- Dhimish, M., Badran, G.: Investigating defects and annual degradation in UK solar PV installations through thermographic and electroluminescent surveys. *npj Mater. Degrad.* 7, 14 (2023)
- Berardone, I., Garcia, J.L., Paggi, M.: Analysis of electroluminescence and infrared thermal images of monocrystalline silicon photovoltaic modules after 20 years of outdoor use in a solar vehicle. *Sol. Energy* 173, 478–486 (2018)
- Muntwyler, U., Schuepbach, E., Lanz, M.: Infrared (IR) drone for quick and cheap PV inspection. In: 31st European Photovoltaic Solar Energy Conference and Exhibition. pp. 1804–1806 (2015)
- Gallardo-Saavedra, S., Hernandez-Callejo, L., Duque-Perez, O.: Technological review of the instrumentation used in aerial thermographic inspection of photovoltaic plants. *Renewable Sustainable Energy Rev.* 93, 566–579 (2018)
- Bommes, L., Pickel, T., Buerhop-Lutz, C., et al.: Computer vision tool for detection, mapping, and fault classification of photovoltaics modules in aerial IR videos. *Prog. Photovoltaics Res. Appl.* 29(12), 1236–1251 (2021)
- Rahaman, S., Urmee, T., Parlevliet, D.: PV system defects identification using Remotely Piloted Aircraft (RPA) based infrared (IR) imaging: A review. *Sol. Energy* 206(2–3), 579–595 (2020)
- Álvarez-Tey, G., Jiménez-Castañeda, R., Carpio, J.: Analysis of the configuration and the location of thermographic equipment for the inspection in photovoltaic systems. *Infrared Phys. Technol.* 87, 40–46 (2017)
- Jahn, U., Herz, M., Köntges, M., et al.: Review on infrared and electroluminescence imaging for PV field applications. Report IEA-PVPS T13–10 (2018). https://www.researchgate.net/publication/324703087_Task_13_Review_on_Infrared_and_Electroluminescence_Imaging_for_PV_Field_Applications
- Ma, M.Y., Zhang, Z.X., Liu, H., et al.: Fault diagnosis of crystalline silicon photovoltaic modules based on I-V characteristic analysis. *Acta Energiae Solaris Sin.* 42(06), 130–137 (2021)
- Liu, G., Yu, W.: A fault detection and diagnosis technique for solar system based on Elman neural network. In: 2017 IEEE 2nd Information Technology, Networking, Electronic and Automation Control Conference (ITNEC). Chengdu, China, pp. 473–480 (2017)
- Dunderdale, C., Brettigny, W., Clohessy, C., et al.: Photovoltaic defect classification through thermal infrared imaging using a machine learning approach. *Prog. Photovoltaics Res. Appl.* 28(3), 177–188 (2020)
- Goodfellow, I., Pouget-Abadie, J., Mirza, M., et al.: Generative adversarial nets. In: Proceedings of the 27th International Conference on Neural Information Processing Systems. vol. 2, pp. 2672–2680. Cambridge, MA (2014)
- Ricardo, H., Gttulio, A., Enes, G., et al.: Automatic fault classification in photovoltaic modules using convolutional neural networks. *Renewable Energy* 179(01), 502–516 (2021)
- Bommes, L., et al.: Anomaly detection in IR images of PV modules using supervised contrastive learning. *Prog. Photovoltaics* 6, 30 (2022)
- Maghami, M., Hizam, H., Gomes, C., et al.: Power loss due to soiling on solar panel: A review. *Renewable Sustainable Energy Rev.* 59, 1307–1316 (2016)
- Wu, Y., He, Q., Xue, T., et al.: How to train neural networks for flare removal. In: IEEE/CVF International Conference on Computer Vision (ICCV). Montreal, QC, Canada, pp. 2219–2227 (2021)
- Qiao, X., Hancke, G., Lau, R., et al.: Light source guided single-image flare removal from unpaired data. In: IEEE/CVF International Conference on Computer Vision (ICCV). Montreal, QC, Canada, pp. 4157–4165 (2021)
- International Electrotechnical Commission. IEC/TS 62446-3:2017 Photovoltaic (PV) systems. Requirements for testing, documentation and maintenance—Part 3: Photovoltaic modules and plants—Outdoor infrared thermography (2017)
- Salem, F., Awadallah, M.: Detection and assessment of partial shading in photovoltaic arrays. *J. Electr. Syst. Inf. Technol.* 3, 23–32 (2016)
- Teo, J., Tan, R., Mok, V., et al.: Impact of partial shading on the pv characteristics and the maximum power of a photovoltaic string. *Energies* 11, 1860 (2018)
- Zhao, Y., Huang, H., Li, Z., et al.: Intelligent garbage classification system based on improve MobileNetV3-Large. *Connect. Sci.* 34(1), 1299–1321 (2022)
- LeNail, A.: Nn-svg: Publication-ready neural network architecture schematics. *Open Source Software* 4, 747 (2019)
- Goodfellow, I., Bengio, Y., Courville, A., et al.: Deep Learning. vol. 1, MIT Press Cambridge, Cambridge, MA (2016)
- Li, Y., Yuan, Z., Zheng, K., et al.: A novel detail weighted histogram equalization method for brightness preserving image enhancement based on partial statistic and global mapping model. *IET Image Proc.* 16, 3325 (2022)
- Millendorf, M., Obropta, E., Vadhavkar, N.: Infrared solar module dataset for anomaly detection. In: The International Conference on Learning Representations (ICLR). Addis Ababa, Ethiopia (2020)
- Alfaro, M., Loaiza, C., Franco, M., et al.: Dataset for recognition of snail trails and hot spot failures in monocrystalline Si solar panels. *Data Brief* 26(10), 1–6 (2019)
- Howard, A., Sandler, M., Chen, B., et al.: Searching for MobileNetV3. In: 2019 IEEE/CVF International Conference on Computer Vision (ICCV). Seoul, Korea (South), pp. 1314–1324 (2019)
- Quarter, P., Grimaccia, F., Leva, S., et al.: Light unmanned aerial vehicles (UAVs) for cooperative inspection of PV plants. *IEEE Photovoltaics* 4(4), 1107–1113 (2014)
- Köntges, M., Kurtz, S., Packard, C.E., et al.: Review of Failures of Photovoltaic Modules; Report IEA-PVPS T13-01:2014; International Energy Agency: Paris, France (2014)
- Liang, D., Yang, F., Zhang, T., et al.: Understanding Mixup training methods. *IEEE Access* 6(18), 58774–58783 (2018)
- Qian, S., Ning, C., Hu, Y.: MobileNetV3 for image classification. In: 2021 IEEE 2nd International Conference on Big Data, Artificial Intelligence and Internet of Things Engineering (ICBAIE). Nanchang, China (2021)

37. Chen, P., Jian, Q., Wu, P., et al.: A multi-domain fusion human motion recognition method based on lightweight network. *IEEE Geosci. Remote Sens. Lett.* 19(01), 1–5 (2022)
38. Liu, X., Di, X.: TanhExp: A smooth activation function with high convergence speed for lightweight neural networks. *IET Res. J.* 09(09), 1–7 (2020)
39. Ge, Z., Liu, S., Wang, F., et al.: YOLOX: Exceeding YOLO Series in 2021. *arXiv:2107.08430v2* (2021)

How to cite this article: Tang, C., Ren, H., Xia, J., Wang, F., Lu, J.: Automatic defect identification of PV panels with IR images through unmanned aircraft. *IET Renew. Power Gener.* 17, 3108–3119 (2023).
<https://doi.org/10.1049/rpg2.12831>